Internal structure of dense electrodeposits

Christophe Léger, Juan Elezgaray, and Françoise Argoul
Centre de Recherche Paul-Pascal, CNRS, Avenue Schweitzer, 33600 Pessac, France
(Received 5 October 1999)

We report experimental investigations of the structure of dense patterns obtained during electrochemical deposition of copper in thin cells. The deposit correlation function reveals the periodic structuration of the patterns but shows that the primary spacing is not steady during the growth and that moreover it is not simply related to the diffusion length. Another measurable quantity is the occupancy ratio of the fingers in the cell. Its variation as a function of the experimental parameters is interpreted from specific properties of electrochemical growth. The results are discussed with respect to the well-known behavior of cellular solidification fronts.

PACS number(s): 81.10.Dn, 81.15.Pq, 66.10.−x

I. INTRODUCTION

Among the variety of morphologies which have been recognized since the mid-1980s in electrochemical deposition in a confined cell (thin cell ECD) [1–10] the dense branching morphology seems to have received the most constant interest both experimentally and theoretically [9–22]. Although this type of morphology has been recognized and named in the 1980s by the physicist community, one can find in the older powder electrometallurgy literature [23–25] evidence of dense arrays of elongated fibers, dendrites or whiskers. The dense branching morphology (DBM) is characterized by a densely ramified structure enclosed in a flat (rectangular cells) or radial (circular cells) envelope. Similar morphologies have also been observed in quite different growth systems [26,27], such as Hele-Shaw fingering [28–30], crystallization processes [31,32], bacterial growth [33,34] or combustion [35,36].

In the context of electrochemical deposition, the understanding of DBM has raised fundamental questions that still remain sources of debate. Is it favored by some Ohmic drop (dissipation) inside the branches of the deposit [10–12], or by an isotropic electrochemical kinetics [37]? Do convection processes stabilize these electrochemical patterns? What are the exact roles of natural convection [38,39], electroconvection [40–44] and cellular mixing [19,45,46]? Can it be observed in purely diffusion-limited growth regimes [47,48] or is there a building of a space charge which would explain the selection of these morphologies [18,40–42,49]? Different models of dense branching have been proposed in the literature.

Ohmic models. These models [8,15–19,50] focus exclusively on the transport of ions outside the zones of concentration gradients (diffusion layers), where the transport is driven by migration solely. They are based on the assumption that the interface automatically adjusts its velocity to the migration speed of the anions [17,49] (which do not react on the electrode) to limit the building of a space charge ahead of the deposit. They predict the growth velocities from ion mobilities and the average metal concentration of the deposit, in good agreement with experimental measurements [18].

Diffusive models. These models assume the local electroneutrality inside the electrolyte, beyond the diffuse layer (Debye length). This leads to a diffusion equation for the equivalent concentration field $C=z^+C^+=-z^-C^-$ (z^+, z^- are the charge numbers of the cations and anions, respectively). Its one-dimensional (1D) steady solution in the frame moving with the deposit gives the averaged velocity of the growth and the metal concentration of the deposit [19,47,48]. The fact that both Ohmic and diffusive models converge to the same conclusions is not so surprising afterwards because the relation for the velocity is inferred from the hypothesis of 1D steady-state growth (invariant diffusion length) whatever the existence of a local charged layer at the metal interface. The dynamics of growth is, therefore, completely ascribed to the arrival of cations on the surface of the deposit. Far beyond the diffusion layer, the concentration gradient is null, the transport is driven by migration of ionic species (Ohm's law). Inside the diffusion layer, the evolution equation for the equivalent concentration field is a diffusion equation [47,48,51] and one can relate the shape of the concentration profile (through its diffusion length L_d) to the growth velocity v: $L_d=D/v$ [19,47,48]. 1D diffusive models reproduce perfectly the macrocospic dynamics (transitory and stationary) but cannot capture the internal structuration of the deposit.

Stochastic models (Monte Carlo simulations). More or less sophisticated adaptations of the diffusion-limited-aggregation (DLA) model have been introduced to account for a finite diffusion length and/or specific interactions of the random walkers with the aggregate interface. In 1985, Voss and Tomkiewicz proposed a generalization of DLA with multiple particles and surface sticking probability [52]. Collins and collaborators extended these ideas and analyzed the influence of a finite diffusion length on DLA clusters [53,54]. In 1993, Erlebacher and collaborators defined a migrational envelope surrounding the growing aggregate. Within this envelope, the particle motion is biased toward the nearest point on the aggregate whereas the transport is Brownian outside [55]. More recently, Hill and Alexander [56] proposed a variant including a bias in the random walk to mimic migration (adjustable drift distance) and a global sticking coefficient to account for surface attachment kinetics. These models reproduce globally the average morphological features of the deposits, but provide a very simplified picture of their internal structuration (their multiscale structure will be described in Sec. III A).

Stability analyses. To account for ramifications behind the flat envelope, Grier and co-workers [2,11,12] extended Mul-

lins and Sekerka's stability analysis to electrochemical growth. In these two-sided models, a diffusion field satisfies an anisotropic Laplace's equation within the aggregate envelope, and a diffusion equation (or Laplace's equation in the quasistationary limit) outside. The interface advances with a velocity proportional to the normal gradient of the underlying field. Stability analyses emphasize the role of dissipative and anisotropic current transport in the aggregate, but in linear geometry, a finite diffusion length is necessary to account for the stability of the long-wavelength modes [12]. It is suggested that the marginally stable wavelength depends linearly on the diffusion length. Another approach, advocated in Ref. [57], is based on mean-field modeling of DLA [58]. It involves three different fields (electrolyte concentration, density of the aggregate and electric potential). Full numerical solutions of the 2D equations show that well-defined fingers develop behind a flat envelope. The distance between the fingers is of the order of magnitude of the characteristic scale of the diffusive field. This model accounts for concentration profiles and front velocities observed in experiments.

From an experimental viewpoint, several studies focused on the construction of morphology diagrams to delimit the zone of existence of the dense morphology [2–4,20,50,59]. These diagrams remained very empirical and controversial. Strong discrepancies depending on the experimental constraints can be found in the literature. These discrepancies have been in part attributed to uncontrolled impurities in the solution of metal cations [60–62] but it seems that even in properly conditioned experiments, ECD exhibits a very strong sensitivity to initial conditions which could be intrinsic. Rather than studying morphological transitions from or to DBM, a complementary approach focuses on the evolution of this morphology with respect to experimental parameters. In the case of dense patterns, the mean distance between the branches (the largest correlation length of the mass of the deposit in the direction perpendicular to the velocity) appears as a natural parameter to characterize the morphology. Surprisingly, no quantitative investigation of this characteristic length of the pattern had been published until the recent work of Zik and Moses [35]. In Ref. [35], they extend their conclusions on the wavelength selection in 2D transport-limited combustion [36] to explain the evolution of the mean distance between the branches of dense electrodeposits. Their main physical argument states that the characteristic length of the pattern in the direction perpendicular to the velocity is equal to the diffusion length of the diffusive field. We question this hypothesis hereafter.

In this paper, we focus on dense branched morphologies (DBM) obtained by electrochemical deposition of copper in very thin cells (50 μm) where natural convection is negligible [39,63–65]. On scales larger than the Debye length, the assumption of local electroneutrality leads to a simple diffusion equation [51] that we have checked using interferometric measurements of the metal cation concentration field [63]. In thin cells, we have recognized a (j, C^{∞}) parameter domain (j being the mean current density, C^{∞} being the bulk concentration) where parameter domain where the growth process is diffusion limited (in which convective processes are negligible). In this parameter zone, depending on the counteranion (sulfate, acetate, nitrate, chloride), we have observed different growth regimes [48,66] from sparse ramified growth to DBM. Hereafter, our discussion focuses essentially on these diffusion-limited DBM. We propose a characterization of their internal branching structure.

Section II is devoted to experimental aspects and Section III starts by a description of DBM, focusing on the different length scales involved in thin cell ECD. We recall the global 1D diffusion model which has been proposed in the literature to describe macroscopic (millimetric) 1D features such as growth velocity, average metal concentration inside the deposit, and concentration profiles [47,48]. We consider also a smaller scale (tens of μm) local growth dynamics and we report here an experimental check of the interfacial relation between the local velocity and the concentration gradient in two dimensions. Section IV deals with the characterization of the periodicity (aperiodicity) of the branched structure of DBM based on the computation of correlation functions of the deposit. We show that whereas the wavelength λ of the pattern is of the same order of magnitude as the diffusion length, they are not simply related. However, the occupancy ratio Θ (defined as the proportion of the cell width occupied by the deposit) behaves linearly with the bulk concentration and does not depend on the diffusion length. Finally, by extending the conclusions of our study of diffusion-limited DBM to growth in thicker cells (involving natural convection), we stress again the role of confinement on the hierarchical structuration of DBM.

II. EXPERIMENTAL

The confinement of the electrolyte in a thin cell is done in a linear geometry, the cathode and the anode being parallel to each other, and perpendicular to the direction of growth. The electrochemical cell is made of two closely spaced optical glass plates ($\lambda/4$ flatness over 50×50 mm^2), sandwiching the electrolyte. The gap e between the two plates is fixed to 50 μm in the experiments discussed here, except for the last one discussed in Sec. IV D. Two straight parallel ultrapure copper (anode) and silver (cathode) wires (50 μm diameter, GoodFellow 99.99% purity) are tightly confined between the two glass plates and play also the role of spacers. The cell is filled with the electrolyte by capillarity. The solutions of copper acetate or copper nitrate are prepared from deionized water and 99% purity salts provided by Aldrich. With copper nitrate, 1% $CuCl_2$ is added to the $Cu(NO_3)_2$ electrolyte to avoid the passivation of the cathode with copper hydroxide prior to the onset of the growth. With copper acetate, the anodic part of the cell is filled by a dilute solution to avoid the precipitation of the salt due to saturation effects by dissolution of the anode. Prior to use, all these solutions are carefully cleaned of any trace of dissolved oxygen by bubbling nitrogen through them for 1 h. ECD experiments are performed at fixed current (galvanostatic) and at room temperature ($\approx 20\,^{\circ}C$), in a two-electrode configuration, and the voltage drop $\phi_{\text{anode}} - \phi_{\text{cathode}}$ is recorded simultaneously. The cathode, where the reduction occurs, is depleted in metal cations as soon as the current is set. By convention, the sign of reduction currents is negative.

The measurements of the electrolyte concentration have been performed with a two-beam interferometric device, on which a phase modulation of the reference wavefront was added to extract the 2D concentration field with a temporal

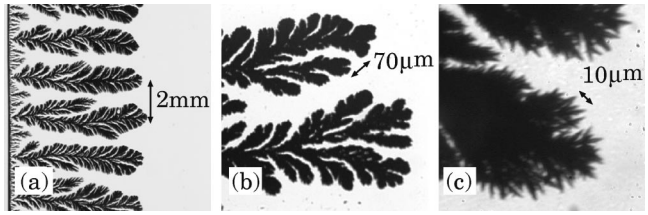

FIG. 1. Photographs of a copper deposit at different scales. Parameters: $[Cu(NO_3)_2]=0.5$ mol l^{-1}, $j=$ 50 mA cm^{-2}.

resolution of a fraction of one second and a spatial resolution of about 10 μm. A detailed description of the phase-shift Mach Zehnder interferometer can be found in Refs. [63,67]. The interference patterns are grabbed through a camera, coupled to a digitizing system [68] for further analysis. The principle of temporal phase-shift interferometry [69] consists of computing the complete 2D phase field from a finite set of interference pictures with shifted reference wavefronts. The concentration field is afterwards straightforwardly determined from this phase field. The gray scale or contour lines coding of the electrolyte concentration shown in the figures of this article have all been obtained with this technique. In a typical experiment, the noise amplitude in the 2D phase map measurement is about $\pi/50$. This corresponds to a concentration difference equal to 10^{-2} mol l^{-1} in our confined cells (50 μm gap). The signal-to-noise ratio can be increased by averaging the concentration field along a direction parallel to the cathode, resulting in 1D concentration profiles. Despite the fact that the experimental errors on the concentration depend on the relative errors on cell spacing and bulk concentration, the measured concentration drop between the bulk and the dead part of the deposit (where the electrolyte is expected to be completely depleted) was always equal to the bulk concentration within 2%. This gives an upper bound to the experimental error. The reader may find in Ref. [69] a comprehensive presentation of phase-shift interferometry. The different phase-shift techniques as well as their relative accuracies are extensively discussed in that review.

III. GENERAL FEATURES OF DBM IN THIN ECD CELLS

A. Multiscales of DBM

The microscopic texture of these deposits is illustrated at different scales in Fig. 1. Comparing the different panels of this figure, the transformation of the bunch of very sharp needles in (c) into a rounded finger in (b) is quite remarkable. The largest picture in (a) is even more surprising since again the preceding small fingers have collapsed to form a bigger finger 20 times larger. This hierarchical organization of the deposit is a very general feature in thin cell ECD. Its characteristic scales are undoubtedly determined by the confinement of the growth. The first scale is related to the sharpness of the needles (submicron size). Around these small needles the transport by diffusion is three-dimensional and therefore its extension is limited in space. The spatial confinement of the 3D diffusion layer is produced by the sharpness of the needle itself, and may explain that at this scale the needles get very close to each other and fill the interspace between the glass plates. The second scale is given by the distance between the plates of the electrochemical cell (50 μm). This gap spacing corresponds roughly to the width of the small finger [Fig. 1(c)]. For these fingers, which fill the gap between the glass plates, the transport is quasi-two-dimensional since they have a characteristic width of a few tens of microns [see Fig. 1(b)]. The screening diffusion process between these small fingers produces a branched pattern such that the distance between the fingers is about twice their width, very reminiscent of a Hele-Shaw fingering pattern [27]. The formation of separate fingers from bunches of needles is evidence of diffusive screening [57]. In Fig. 1(a) the fingers are again assembled in branches of mm width. That is the scale we will focus on here, by characterizing the average distance between these branches (the wavelength λ of the pattern) and their occupancy ratio in the cell.

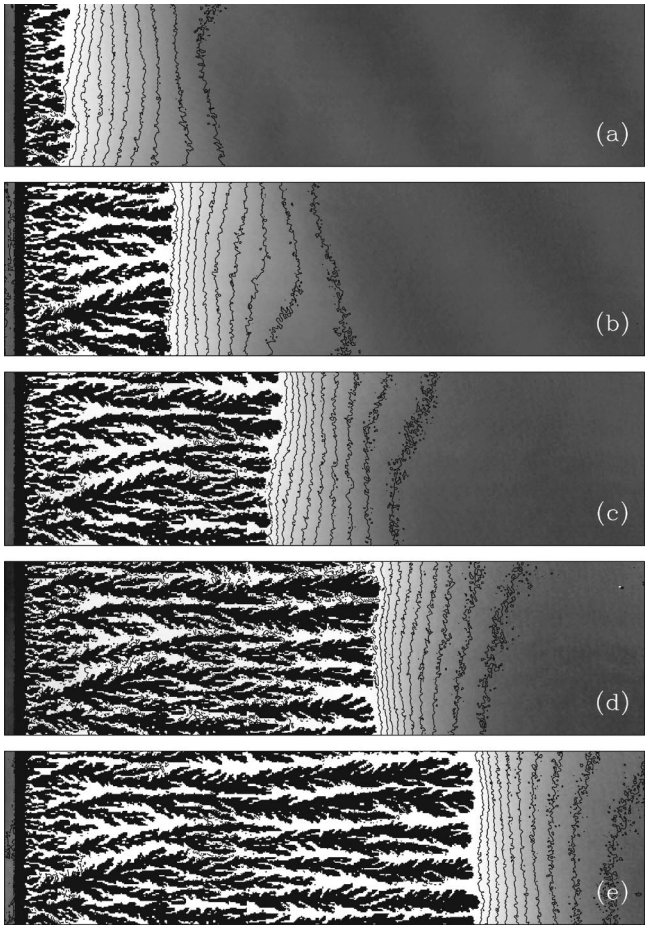

FIG. 2. Dense 1D growth by ECD from a cupric acetate solution in thin cell. On each panel we plot the deposit (in black on the left) together with the concentration field measured by interferometry (contour lines + grey level coding with black corresponding to the initial bulk concentration C^{∞} and white to a null concentration). The concentration difference between two contour lines is approximately $C^{\infty}/10$. Parameters: $[Cu(CH_3COO)_2]=0.2$ mol l^{-1}, $j=12$ mA cm^{-2}. The time interval between two successive pictures is 880 s. Scale of the pictures: 5.4×1.7 mm^2.

B. Stationary 1D growth regimes

Figure 2 illustrates the spatial and temporal dynamics of a DBM process. Each picture of this figure shows the black deposit (on the left) and the 2D concentration field coded in gray and its contour lines (on the right). The time interval

between two pictures is constant. This dense branched aggregate is bounded by a flat linear front which invades the cell at constant velocity, pushing away the depleted diffusion layer whose size remains constant. This stationary growth regime has been modeled macroscopically by a diffusive 1D model. The equation for the stationary equivalent concentration profile in the frame moving with the interface reads [19,47,48]:

$$C(\zeta)=C^{\infty}+(C^{0}-C^{\infty})\exp\left(-\frac{\zeta}{L_d}\right). \tag{1}$$

$\zeta=x-vt$ is the distance to the deposit front, x is the laboratory coordinate, v is the velocity of the growth along the direction x, $C^{0}=C(\zeta=0)$, C^{∞} is the initial concentration (bulk equivalent concentration). The diffusion length $L_d=D/v$ is the natural length scale for the spreading of the diffusion layer in front of the moving deposit (D is the ambipolar diffusion coefficient).

DBM is generally defined empirically as reminded in the introductory section. We propose here a basis for a more rigourous definition in the following terms: the term DBM will be relevant if the mean distance λ between the branches is of the order of magnitude or smaller than the size of the depleted layer. This criterion implies that the ions do not penetrate significantly between the fingers, and that the concentration field is roughly one-dimensional. As counter examples, the reader may look at Figs. 13(a) in Ref. [48] and 2(b) in Ref. [70].

From Eq. (1) and the interfacial boundary relation for the current density j, $j(1-t_+)/F=-D\partial_x C|_{\zeta=0}-C^{0}v$ [47,48], the expression for the constant interfacial velocity with respect to j and C^{∞} reads

$$v=-\frac{j(1-t_+)}{FC^{\infty}}, \tag{2}$$

t_+ is the transference number of the cation Cu^{2+}, F is the Faraday constant. The metal concentration inside the deposit ρ_{1D} is straightforwardly deduced from the conservation equation at $\zeta=0$:

$$\rho_{1D}v=\frac{D}{(1-t_+)}\partial_x C|_{\zeta=0}+\frac{C^{0}v}{(1-t_+)}, \tag{3}$$

which implies that

$$\rho_{1D}=\frac{C^{\infty}}{1-t_+}. \tag{4}$$

ρ_{1D} is the average concentration of metal atom along the y direction, perpendicular to the growth direction x. It depends only on the bulk concentration of metal cations. In the case of stationary 1D growth, ρ_{1D} is an invariant of the growth which quantifies the average porosity of the deposit. Without supporting electrolytes, in solution, the transference number of copper ranges between 0.2 and 0.5, depending on the anion. Therefore, the metal concentration behind the flat envelope will not be greater than twice the initial concentration in copper cations: it is much smaller than the concentration of metal copper ($\approx 150\ \mathrm{mol\,l^{-1}}$). Our black and white coding of the ECD clusters (such as in Fig. 2) is therefore strongly misleading, since the deposit is not at all plain copper metal but rather a highly porous phase made of nanometer scale needles of copper (as illustrated in Fig. 1).

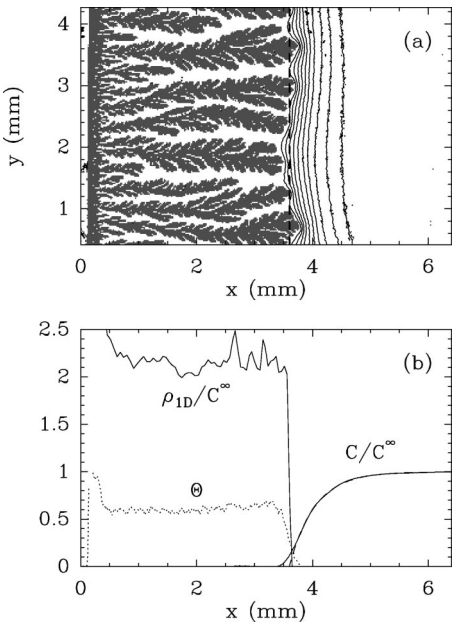

FIG. 3. One-dimensional characterization of the dense growth. (a) Picture of the deposit (in grey) and representation of the concentration field with contour lines. The vertical dashed line shows the position of the effective front determined by extrapolation of the exponential shape of the diffusion layer [Eq. (1)]. (b) 1D concentration profiles of ''Cu'' in the different phases. Plain line on the left: copper atom concentration inside the deposit (averaged over the cell width). Plain line on the right: cupric ion concentration in the diffusion layer. Dotted line on the left: ''occupancy ratio'' Θ of the deposit (see text).

Figure 3 presents the 1D features of dense patterns in ECD. It shows the different profiles which can be extracted from a particular picture of the deposit and its 2D concentration map. In (a) we recognize the deposit in gray with the contour lines of the concentration field, between two close lines there is a concentration difference of about $C^{\infty}/10$. The vertical dashed line marks the position of the effective front $\zeta=0$, extrapolated from the exponential shape of the concentration profile [Eq. (1)]. Figure 3(b) reports three 1D concentration profiles. The right curve (plain line) corresponds to the concentration of cations inside the electrolyte averaged along the direction parallel to the front. The top left curve (plain line) corresponds to the 1D average concentration of metal copper ρ_{1D} inside the deposit. The bottom left curve (dotted line) corresponds to the occupancy ratio Θ, defined below.

ρ_{1D} was computed from conservation Eq. (3). The front velocity v was estimated directly from successive pictures of the deposit, and $\partial_x C|_{\zeta=0}$ was computed from the ratio C^{∞}/L_d [in the experiment C^{0} is negligible versus C^{∞}, as shown in Fig. 3(b)]. L_d was obtained by fitting the experimental 1D concentration profiles with Eq. (1) [dashed line on the right part of Fig. 3(b)]. Equation (3) therefore reads $\rho_{1D}/C^{\infty}=D/[(1-t_+)vL_d]$. In Fig. 3(b) ρ_{1D}/C^{∞} rapidly converges to $(1-t_+)^{-1}\approx 2$, as predicted by Eq. (4).

The occupation ratio Θ [dotted line in Fig. 3(b)] is the

fraction of the space occupied by the (porous) metal deposit. Its measurement involves a threshold of the picture of the deposit captured by the frame grabber, Θ being defined as the number of pixels above the threshold divided by the width of the picture. The value of Θ depends on the choice of the threshold, nevertheless we have checked that this choice did not change the behavior of Θ with respect to j or C^{∞}, as discussed in Sec. IV C.

C. Finger growth velocity

The 1D model presented in the previous section predicts the front velocity, the mean concentration profiles and the average metal concentration ρ_{1D}. However, it gives no insight into the internal structuration of the deposit zone (i.e., distribution of the metallic atoms behind the smooth envelope) and does not propose any prediction for the growth velocity of the individual fingers or their metal content. In this section, we investigate the evolution equation for the fingers by analyzing the link between the local growth velocity and the surrounding 2D concentration field.

The mass conservation of metal species on the finger boundary reads

$$\rho_{2D}\vec{v}\cdot\vec{n}=\frac{D}{(1-t_+)}\vec{\nabla}C\cdot\vec{n}, \tag{5}$$

where $\vec{n}$ is the unit vector normal to the interface, directed toward the bulk, ρ_{2D} is the local metal concentration inside a finger. This concentration is greater than ρ_{1D} since

$$\rho_{1D}=\Theta\rho_{2D} \tag{6}$$

and $0<\Theta<1$.

Equation (5) assumes implicitly that convective fluxes are negligible so that the transport of electroactive species is diffusive. Natural convection is negligible in the very thin cells used here [63,65], and electroconvection should be revealed by characteristic arches in the concentration map [40] which are invisible in all the experiments we describe here. In solidification processes, the local linear relation between the velocity and the temperature gradient derives naturally from heat conservation at the interface. The situation is different here since the porosity of the finger (ρ_{2D}) is *a priori* unknown and could depend on the local current density.

Our interferometric setup can be used to measure independently the normal velocity of the aggregate and the concentration gradient at the interface, to check the validity of relation (5). The principle of the method is illustrated in Fig. 4. On each pixel of the contour of the deposit, the normal concentration gradient is estimated from the 2D concentration map. In Fig. 4 this concentration field is coded by discrete gray levels. The normal velocity is given by the distance between two consecutive contours of the deposit, projected onto the normal to the interface. The representation of the normal velocities by arrows on the contour of a selected zone of the deposit is very suggestive of the dynamics of the growth. It provides a direct evidence for the distribution of the interfacial current densities and shows that a major part of the current flows on the tip of the branches, in a narrow front zone of the deposit where the concentration gradient is nonzero.

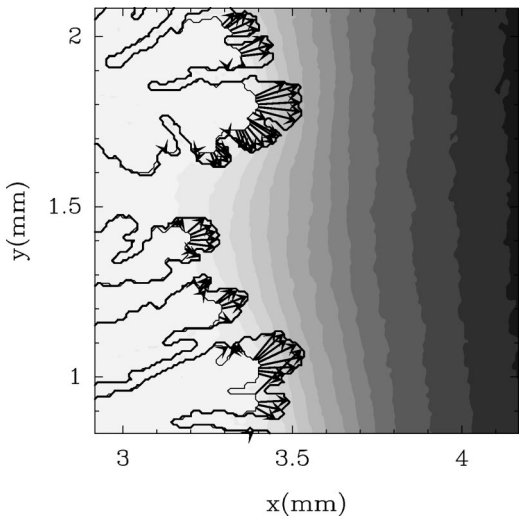

FIG. 4. Illustration of the computation method of the normal velocities from experimental data. Two successive contours of the deposit during its growth are shown ($t\approx1040$ s, $\Delta t\approx48$ s). The concentration field corresponding to the first snapshot is coded using discrete grey levels (same coding as for Fig. 1). The arrows show the computed normal velocities. Parameters: $[Cu(NO_3)_2]=0.5$ mol l^{-1}, $j=50$ mA cm^{-2}. Scale of the picture: 5×7 mm^2.

The discretization of time and space in the analysis introduces two sources of errors. On the one side the distance between two successive contours has to be larger than a few pixels to enable the velocity measurement, whereas the linear relation between the normal velocity and the normal concentration gradient [Eq. (5)] breaks down when the time interval for integration is too large. On the other side the determination of the normal direction is spoiled by the uncertainty of the contour detection. The combination of these effects produces artificial crossovers between adjacent velocity vectors, as shown in Fig. 4. In the program which computes the velocity vectors, some tests have been implemented to remove unexpected data. In particular, when the noise level on the concentration gradient produces unrealistic values, the estimated velocity vectors have been omitted in the analysis and deleted from Fig. 4. However, to strengthen the validity of our analysis, we have checked that the experimental results shown in Fig. 5 are independent of the time interval Δt, in a finite range.

Figure 5(a) reports the plots of these normal velocities estimated on the boundary of the fingers versus the normal concentration gradient (averaged on the time interval). We note that all the points, obtained from galvanostatic ECD from copper nitrate at successive times, are distributed along a band parallel to a straight line (in plain) going through the origin. This strongly supports the invariance of ρ_{2D} along the boundary. The slope of the experimental linear behavior can be interpreted from Eqs. (5) and (6). We estimated $\Theta\approx0.62$ from digitized pictures of the pattern. With $D=1.03\times10^{-5}$ $cm^2\,s^{-1}$ [66] and $C^{\infty}=0.5$ mol l^{-1}, one obtains $D\Theta/C^{\infty}\approx1.3\times10^{-3}$ $cm^3\,s^{-1}\,mol^{-1}$. This prediction is plotted with a plain line in Fig. 5(a). The shift of the cloud of points in Fig. 5(a) with respect to the theoretical prediction is certainly due to the discretization of the digitized cluster boundary. This plot strongly supports the local diffusion-limited conservation Eq. (5).

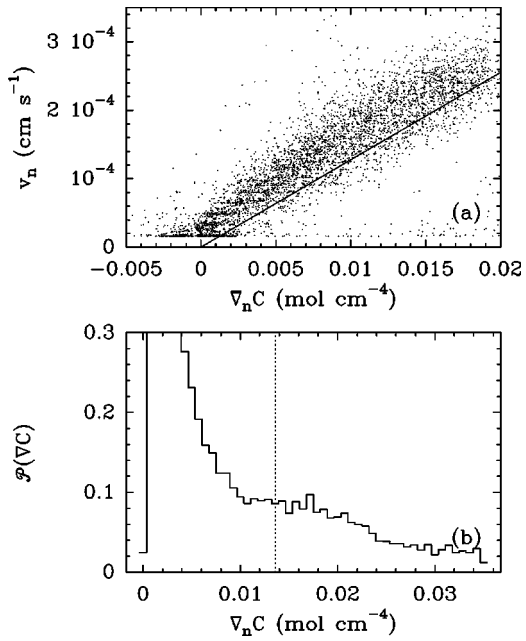

FIG. 5. Plot of the normal velocities versus the normal concentration gradients for the experiment of Fig. 4. The plain line is the prediction of Eq. (5). (b) Histogram of the gradients measured along the interface. The dotted line marks the value of the 1D gradient (C^{∞}/L_d).

In the literature, the hypothesis of diffusion-limited growth has often been deduced *a posteriori* from the analysis of the ramified deposit morphology by comparing its (global) fractal dimension to that of DLA. In a recent work, Argoul *et al.* [71] compared the local velocity of an electroless DLA-like aggregate to its harmonic measure (the normal gradient of an hypothetic Laplacian field surrounding the deposit). To the best of our knowledge, it was the first attempt to characterize the local dynamics of an electrochemical interface. The work presented here is definitely a step beyond, since the diffusion-limited dynamics is directly inferred from independent measurements of local velocities and gradients.

The histogram of the interfacial concentration gradients is plotted in Fig. 5(b), together with the value of the 1D interfacial gradient $\partial_x C|_{\zeta=0}=C^{\infty}/L_d$ in dotted line. This histogram increases very rapidly for low concentration gradients and exhibits a plateau around 0.015 $\mathrm{mol\,cm^{-4}}$, which corresponds to the 1D estimation. The strong divergence of this histogram at low velocities is not significant since it is measured on the ''dead'' part of the deposit, behind the front, where the concentration gradients are close to zero. Figure 5(b) shows that the 1D average of the growth is not an upper bound of the interfacial velocity but rather lies in the middle of the interfacial velocity histogram. Let the local diffusion length l_d be defined as the ratio between C^{∞} and the local gradient. The dispersion of the concentration gradients ($[0.01–0.04]$ $\mathrm{mol\,cm^{-4}}$) gives an estimate of the dispersion of the diffusion length on the interface of the deposit: $\Delta l_d/L_d=\Delta(\nabla_n C)/\partial_x C|_{\zeta=0}\leqslant 1$. We reach the conclusion that the dispersion of l_d is of the same order as or lower than L_d. This result could have been guessed directly from the observation of a DBM picture such as Fig. 2(a): the fluctuations of the branch heights are bounded by the diffusion length L_d. This intuitive observation has been quantified by our local analysis.

At this point we go back to our previous definition of DBM, based on the comparison of λ with L_d, to include the distribution width of the height of the branches Δh. The landmarks of DBM may, therefore, be written as

$$\lambda \leqslant L_d \quad \text{and} \quad \Delta h \leqslant L_d . \tag{7}$$

To conclude this section, we need to check the coherence of our analysis. We have *a priori* assumed that in our thin cell, the ECD process could be considered as two-dimensional at the scale of our observations. The minimal local diffusion length $l_d^{\min}$ (the ratio of C^{∞} over the maximal gradient) is about 0.5×10^{-3} $\mathrm{mol\,cm^{-3}}/2\times10^{-2}$ $\mathrm{mol\,cm^{-4}}\approx 250$ μm. The fact that it remains much larger than the gap between the two glass plates supports our hypothesis.

Finally, the 1D approximation discussed in the previous section is also corroborated by the observations of the confinement of the growing zone inside a narrow band localized at the front of the deposit. This band corresponds also to the zone of fluctuations of the branch heights. It seems, therefore, that the two characteristic scales of DBM, λ and Δh, could be related in some way to the diffusion length L_d. In the next section, we focus on this question through a careful characterization of the internal structure of the deposit.

IV. CHARACTERIZATION OF THE INTERNAL STRUCTURE OF DBM

We now develop an original approach aimed at characterizing the macroscopic (>0.1 mm) internal structure, i.e., the periodic (or aperiodic) organization of the branches of DBM. This analysis relies on the computation of a correlation function which provides a statistical estimate of the mean distance λ between branches.

A. Macroscopic wavelength measurement

From a thresholded picture of the deposit, such as shown in Fig. 6(a), we define $\mathcal{M}(x,y)$ as the ''black and white'' 2D projection of the deposit, $\mathcal{M}(x,y)=1$ on the deposit, $\mathcal{M}(x,y)=0$ elsewhere. This measure has *a priori* nothing in common with the real concentration of metal atoms inside the deposit. It is a 2D macroscopic quantity characterizing the ECD cluster. The correlation function is defined by

$$\mathcal{C}(x,l)=\frac{1}{L_y}\int_0^{L_y}\mathcal{M}(x,y)\times\mathcal{M}(x,y+l)\,dy - \left(\frac{1}{L_y}\int_0^{L_y}\mathcal{M}(x,y)\,dy\right)^2, \tag{8}$$

where L_y is the width of the picture along the y direction. The abscissa of the maxima of $\mathcal{C}(x,l)$, for a fixed value of x, characterize the periodicity (wavelength λ) of the 2D cluster along the direction y perpendicular to the growth direction. A discrete version of Eq. (8) has been applied for the computation of $\mathcal{C}(x,l)$:

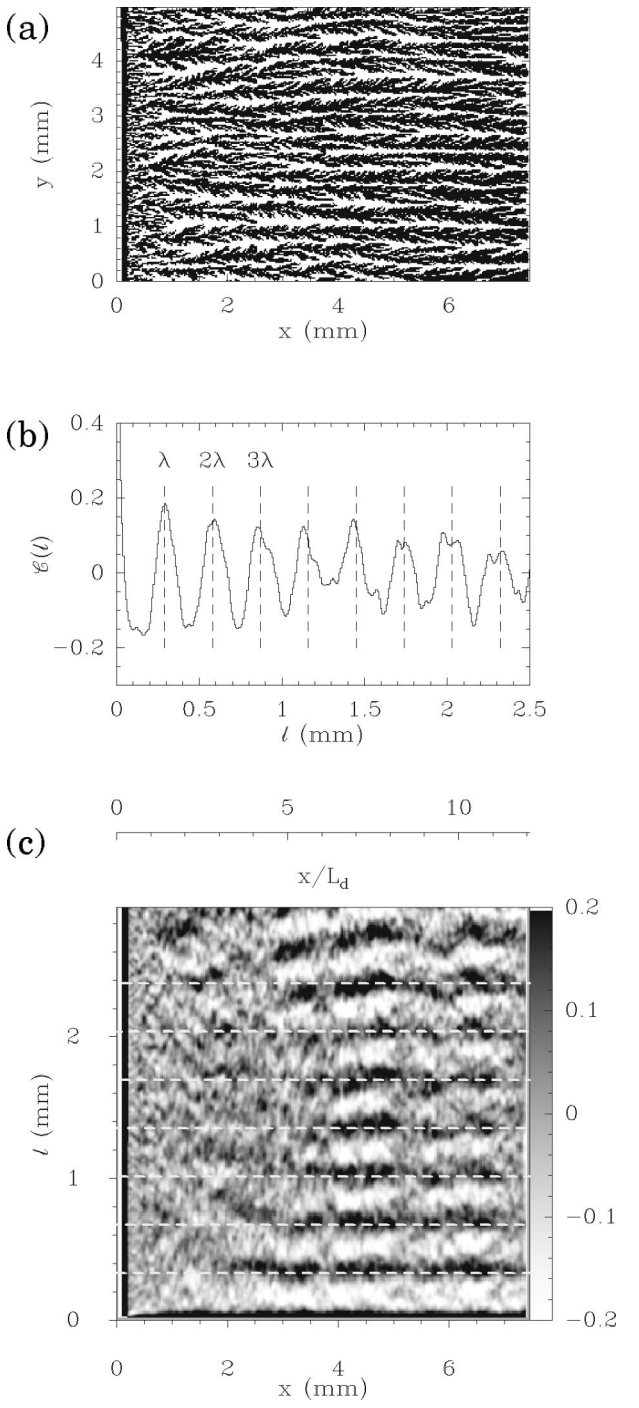

FIG. 6. Illustration of the method of computing the deposit's wavelength. (a) Thresholded picture of the deposit. (b) 1D correlation function of the thresholded picture of the deposit, along the y direction, computed according to Eq. (9), with $x \approx 4.5$ mm. In (c) we check the stationarity of this periodicity by plotting the 2D correlation function. $\lambda \approx 290$ μm. Parameters: $[Cu(CH_3COO)_2] = 0.2$ mol l^{-1}, $j = 12$ mA cm^{-2}.

$$\mathcal{C}(x,l) = \frac{1}{N_y - l} \sum_{y=1}^{y=N_y-l} \mathcal{M}(x,y) \times \mathcal{M}(x,y+l) - \left(\frac{1}{N_y} \sum_{y=1}^{y=N_y} \mathcal{M}(x,y) \right)^2, \quad (9)$$

where N_y is the number of pixels of the width of the picture, $\Theta(x) = (1/N_y) \Sigma_{y=1}^{y=Ny} \mathcal{M}(x,y)$.

The 1D correlation function $\mathcal{C}(x = 4.5 \text{ mm}, l)$ computed from the cluster picture of Fig. 6(a) is represented in Fig. 6(b). We observe that at this position, the lateral structure of the deposit is periodic with a wavelength $\lambda \approx 290$ μm.

To check the stationarity of the morphology, we compute this correlation function for each value x. The fact that the growing zone of the deposit is limited to the foremost part of the branches (as seen in Fig. 4) allows us to use this correlation function as a time record of the growth morphology. Since the structure of the deposit keeps the whole memory of the growth history, this analysis in terms of the correlation function in (x,l) variables sheds light on the temporal evolution of the periodicity of the structure. A gray coding of $\mathcal{C}(x,l)$ as a function of the variables (x,l) is shown in Fig. 6(c). The maxima of the correlation function are coded in black and the minima are coded in white [see the look-up-table on the right side of Fig. 6(c)]. Above each picture of the correlation functions, we add an axis labeled in x/L_d units. Except in the initial transients [48], this representation may be considered as a space-time map and used to characterize the time of settling of a periodic structure and its duration. The spatial axis x/L_d would then be assimilated to a time axis t/t_d with $t_d = D/v^2$ the diffusion time.

Figure 6(c) is a clear illustration of the existence of periodic stationary solutions in DBM. Around 3.8 mm, the structure is locked in a periodic spatial solution which extends over the whole picture (long-range correlations). The transition from aperiodic to periodic structure takes about five diffusion times. The parallel white dashed lines are drawn to stress the maxima of the correlation function. This picture shows that the pattern is highly periodic, and demonstrates the stationarity of the morphology during the growth process. However, we demonstrate hereafter that this behavior is not robust.

Figure 7 shows two distinct space-time correlation pictures which demonstrate the nonstationarity of the internal structure of DBM. The left panels (a) and (b) of Fig. 7 correspond to the same parameters as those of Fig. 6 and we remark that the transition to spatial periodicity takes about the same time ($\approx 4 t_d$). In that example, the periodicity is not conserved in time. Between 4 t_d and 8 t_d, the wavelength is continuously decreasing (as shown by the white dashed line). After 8 t_d, the spatial periodicity is lost and does not seem to come back during that stage of the experiment. We observe the shrinking of the wavelength until the correlation function is overwhelmed with the noise.

The deposit shown in Figs. 7(c) and 7(d) has been obtained for different parameters. Figure 7(d) shows that periodicity disappears suddenly and comes back after a short interval with a smaller wavelength. The distances between the parallel dashed lines drawn in Fig. 7(d) are, respectively, 0.193 and 0.184 mm. This decrease of λ corresponds roughly to the addition of one branch over the width of the picture in Fig. 7(c). Note that the splitting of a branch can be distinguished around $x = 4.7$, $y = 2.9$ mm on Fig. 7(c). In both cases, despite the internal modification of the structure of the deposit, the velocity of the front and the exponential decay of the concentration profile remain constant.

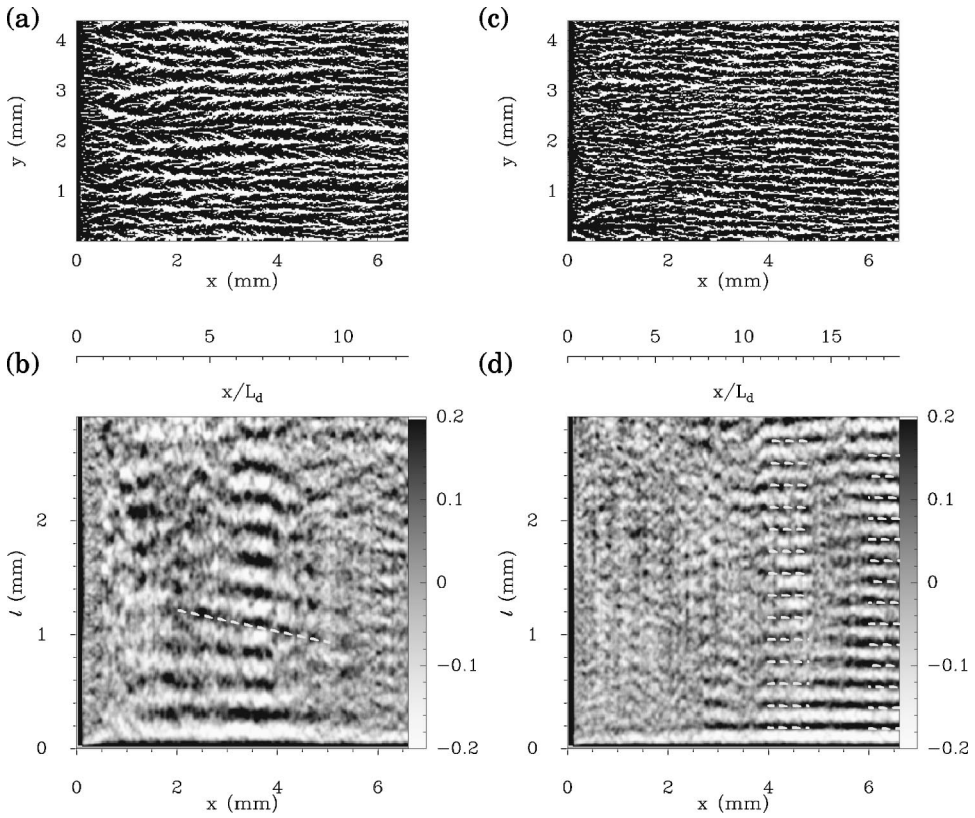

FIG. 7. Evidence for the nonstationarity of the dense pattern wavelengths. (a) and (c) thresholded pictures of deposits obtained from $[Cu(CH_3COO)_2] = 0.2\ mol\,l^{-1}$ at $j=12\ mA\,cm^{-2}$ and $20\ mA\,cm^{-2}$, respectively. (b) and (d) corresponding 2D correlation functions.

The sensitivity of the growth dynamics for a given set of parameters [Figs. 6, 7(a), and 7(b)] and the intermittent character of the spatial periodicity [Figs. 7(c) and 7(d)] provide evidence for the possible coexistence of an infinite set of periodic spatial solutions for the same experimental parameters. This behavior is not really surprising in the context of out-of-equilibrium growth. In particular, during the last few years, there have been experimental results indicating that stable cellular patterns are observed over a finite wavelength range during solidification of alloys and that no wavelength selection occurs [72–75]. Moreover the spacing λ, measured as the distance between two adjacent liquid grooves can vary along the solidification front. The latter feature would manifest itself in the disappearance of the periodicity in our correlation function analysis but our evidence is not sufficient to reach such a conclusion. With respect to solidification processes, electrodeposition mechanisms involve, in addition, the electric field. One could speculate that this factor could explain the long-range periodicity highlighted by our correlation function analysis of DBM.

B. Evolution of the wavelength with respect to the diffusion length

In Fig. 8, we collect the results obtained with different currents and electrolyte (copper acetate) concentrations. The diffusion lengths were computed from the ratio D/v with $D=6\times10^{-6}\ cm^2\,s^{-1}$. This ratio has previously been shown to fit accurately the characteristic length of the diffusion layer [48]. Since the wavelengths may be unsteady during the growth, each point corresponds to a mean of the wavelengths measured during one run. In some cases, an error bar parallel to the λ axis shows the dispersion of the wavelengths.

In Fig. 8(a), we have selected the points corresponding to the same concentration as for Figs. 6 and 7. Figure 8(a) shows that the wavelength of the DBM structure is always of the same order as the diffusion length. However, it is rather difficult to assert that λ is increasing linearly with L_d as

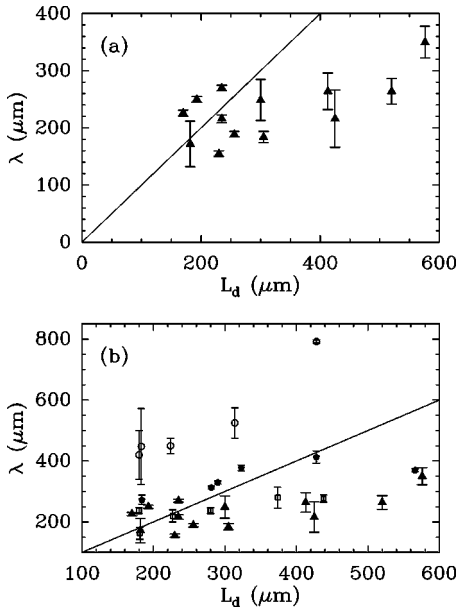

FIG. 8. Evolution of λ as a function of L_d for a set of different experiments performed for different $[Cu(CH_3COO)_2]$: $0.2\ mol\,l^{-1}$ (black triangles), $0.165\ mol\,l^{-1}$ (white squares), $0.135\ mol\,l^{-1}$ (black pentagons), $0.1\ mol\,l^{-1}$ (white circles). L_d has been computed from the relation $L_d=D/v$. The current density used in each experiment can be deduced from the relation $j=-DFC^{\infty}/[L_d(1-t_+)]$.

proposed by Zik and Moses [35] [their prediction is reported in Fig. 8(a)]. On the contrary λ does not change much with L_d, although it remains of the same order as L_d.

In Fig. 8(b), we gather experimental measurements performed at four different concentrations from 0.2 to 0.1 mol l^{-1}, the smaller the concentration, the larger the wavelength for a given diffusion length. The main conclusion from this figure is that λ does not depend on the current density but rather on the bulk concentration C^{∞}. This is consistent with our general observations, namely that the morphology of the deposit is essentially determined by the electrolyte composition (concentration and choice of the cation and the anion). For a given salt, the morphology is mostly dependent on the bulk concentration and weakly dependent on the current density (as far as the current is low enough to exclude electroconvective processes). Zik and Moses' morphological diagram in the (C^{∞},j) plane [20] supports our observations since the lines delimiting the different morphologies are roughly parallel to the j axis.

The evolution of λ with the concentration is illustrated by four pictures of the copper clusters in Fig. 9. The increase of λ when the concentration of the metal cation electrolyte decreases [from (a) to (d)] is quite obvious, whereas the diffusion length does not change much (the contour lines reported on each of these figures are separated by $C^{\infty}/10$). Note that on the last pattern (d) of this figure the contour lines are less straight than the others. This effect has no physical meaning, it is an artifact due to the computation of the optical phase because the electrolyte concentration is rather small. Figure 9 provides unambiguous evidence that, even for a given electrolyte, the diffusion length is not the single parameter that determines the overall morphology.

C. Occupancy ratio

In order to characterize these dense patterns, the width w of the branches may also be computed. Since the fingers are ramified (Fig. 9), their mean width cannot be directly measured. This would require us to define a stem of each finger and to compute the mean distance of the lateral branches with respect to this stem. However, in a first approximation, the fraction of the space occupied by the porous metallic deposit Θ can be interpreted as the ratio w/λ (this would be exact if the fingers were smooth). Remember that Θ is defined as the ratio of the number of black pixels over the width of the picture. In Fig. 10, we report the evolution of this occupancy ratio with respect to the bulk concentration and the diffusion length.

As for λ we see a strong dependence of Θ with the bulk concentration, it increases linearly with C^{∞}. This variation of Θ with C^{∞}, for a given L_d is evidenced in the four pictures of Fig. 9: the patterns become sparser and sparser when the bulk concentration decreases [from (a) to (d)]. However, Θ does not give a direct information about the metal average concentration ρ_{1D} or the local metal concentration ρ_{2D}. It depends solely on their ratio [Eq. 6]. Since Θ behaves exactly as ρ_{1D} with respect to the bulk concentration $\rho_{1D} \propto C^{\infty}$ [Eq. 4], we conclude that ρ_{2D} does not depend on C^{∞}. From Fig. 9 we compute the ratio: $\Theta/C^{\infty} \approx 3.3$ l mol^{-1}, therefore $\rho_{2D} \approx 0.6$ mol l^{-1} for copper acetate electrolytes,

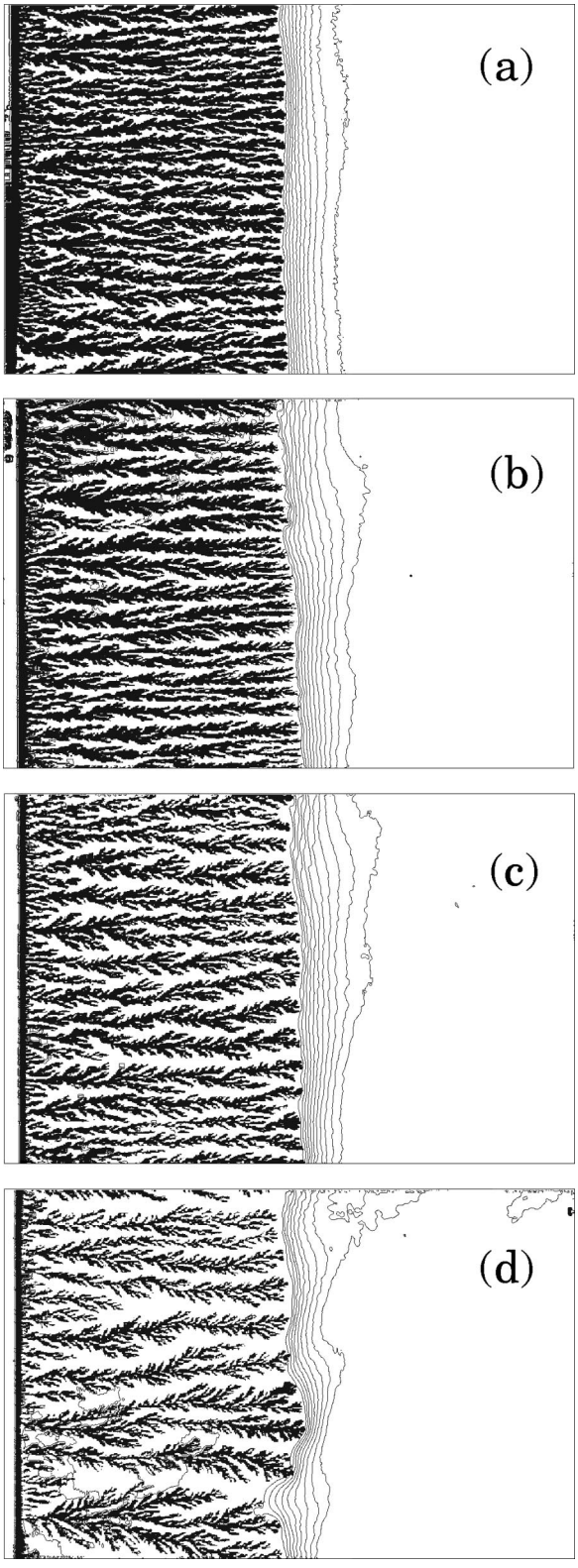

FIG. 9. Illustration of the influence of C^{∞} at fixed L_d on the morphology of copper deposits obtained from $Cu(CH_3COO)_2$ solutions. (a) 0.2 mol l^{-1}, $j=22$ mA cm^{-2}, $L_d \approx 235$ μm, $\lambda \approx 210$ μm. (b) 0.165 mol l^{-1}, $j=20$ mA cm^{-2}, $L_d \approx 275$ μm, $\lambda \approx 245$ μm. (c) 0.135 mol l^{-1}, $j=16$ mA cm^{-2}, $L_d \approx 290$ μm, $\lambda \approx 325$ μm. (d) 0.1 mol l^{-1}, $j=12$ mA cm^{-2}, $L_d \approx 220$ μm, $\lambda \approx 432$ μm.

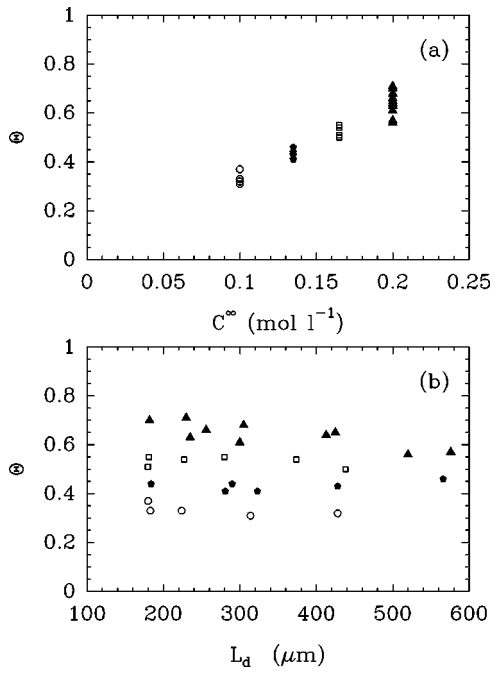

FIG. 10. Evolution of Θ as a function of C^{∞} [in (a)] and as a function of L_d [in (b)] for experiments with different $[Cu(CH_3COO)_2]$: 0.2 mol l^{-1} (black triangles), 0.165 mol l^{-1} (white squares), 0.135 mol l^{-1} (black pentagons), 0.1 mol l^{-1} (white circles).

whatever their bulk concentration within the range [0.1 mol l^{-1}, 0.2 mol l^{-1}].

The essential fact revealed by Fig. 10(a) is the invariance of the metal content ρ_{2D} inside the smallest ramifications of the deposit, independently of the concentration. We demonstrate in Fig. 10(b) that Θ does not depend on the diffusion length L_d. Since the stationary growth solutions of DBM are such that ρ_{1D} does not depend on the current but solely on the concentration, ρ_{2D} does not depend on the current either. This conclusion strengthens our argumentation above, namely that when the current is changed, the width of each branch must change but that the local metal content of each ramification does not change.

This argument is consistent with the measurements reported in Sec. III C. There, we pointed out that the local velocity can be linearly related to the normal gradient only if the local porosity of the fingers does not depend on the local current. This is demonstrated in Fig. 10(b).

In this electrochemical system, the lack of a selected shape results from the fact that only $\rho_{1D}=\Theta\rho_{2D}=C^{\infty}/(1-t_+)$ is imposed. But there are multiple ways to distribute the metal atoms behind the front of the deposit which fulfill this constraint. Even for a given finger width, a deposit made of concentrated fingers with a large gap between them, or dilute tight fingers could satisfy Eq. (4). However, we demonstrate that the metal concentration of the fingers ρ_{2D} is selected. This shape selection criterium is original, it is specific to an ECD process. It can be explained by the fact that the microscopic structure does not depend on the large scale diffusion length but rather on submicroscopic features such as surface kinetics, surface diffusion, charged layer, and micron-scale 3D diffusion.

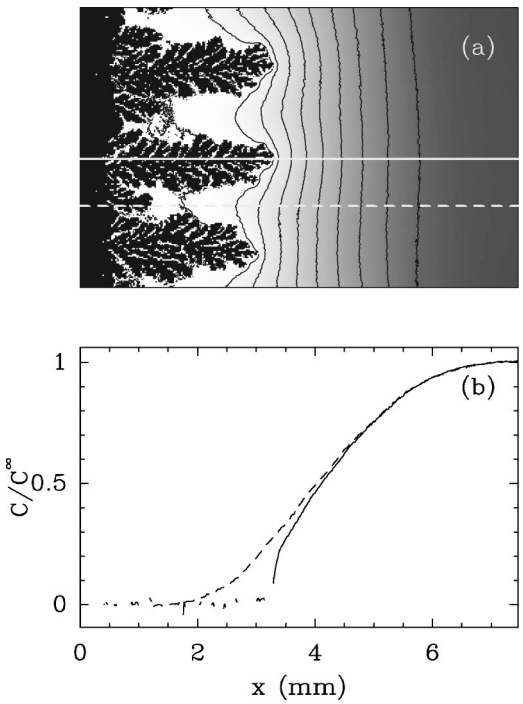

FIG. 11. (a) Deposit and concentration field during the growth of a copper deposit from a cupric sulfate electrolyte in a thick cell ($e=250$ μm). Parameters: $[CuSO_4]=0.2$ mol l^{-1}, $j=8$ mA cm^{-2}. The concentration difference between each contour line is approximately $C^{\infty}/10$. Scale of the figure: 5×7 mm^2. (b) Concentration profiles (averaged along the direction perpendicular to the glass plates) corresponding to the white lines (plain and dashed, respectively) in (a).

D. Generalization to natural convection driven ECD

DBM has also been observed in thicker cells where natural convection contributes to the transport of charged species. Actually, the existence of DBM is a very robust phenomenon in ECD. The onset of natural convection has been interpreted and well documented [38,39,76–82]. Its real influence on the morphology of a thin cell electrodeposit has been more rarely discussed [38,39], in particular with respect to a possible modification of the small and large structure of the deposit.

When the cell gap is greater than about 70 μm [65,63], the existence of concentration gradients close to the electrodes triggers a convective motion of the fluid [39,83]. The size of the convective rolls increases with the square root of time [39,65,70], until the cathodic interfacial concentration gets close to zero and the growth becomes unstable [70,84]. During the subsequent growth, the deposit pushes away a convection-mixed depletion layer whose size is constant for DBM [48]. In Ref. [48], we extended the validity of Eq. (2) for the front velocity to situations where free convection is involved. However, Eq. (1) for the concentration field fails to describe the concentration profile in front of the deposit because the transport is three dimensional around the growing dendrites and two dimensional in the convective rolls. It may therefore be more hazardous to define a diffusion length.

Figure 11 shows a copper cluster obtained from a copper sulfate electrolyte in 250 μm gap cell. The morphology of the deposit is very different from those obtained in 50 μm gap cells, nevertheless this pattern belongs to our description

of DBM. The velocity of the growth becomes constant after a first selection regime [48]. Moreover, the distance between the branches and their height dispersion remain smaller than the size of the depleted zone. We notice that the zone of depletion is much larger than in previous experiments, whereas the growth velocity is nearly the same [as predicted by Eq. (2)]. In this experiment, the front velocity, estimated from successive pictures of the growth is $\approx 1.3\ \mu m\, s^{-1}$. The ratio D/v is therefore ≈ 0.4 mm. The concentration profiles plotted in Fig. 11(b) show that the depleted zone spreads over about 3 mm. It means that in thick cells, the diffusion length D/v is useless to estimate the size of the depleted layer. In Ref. [70] we used an effective diffusoconvective coefficient (greater than the diffusion coefficient) to compare the properties of the convective depleted layer and the predictions of a diffusive model.

An interesting point is that the wavelength of the deposit structure (≈ 1.7 mm), remains of the same order of magnitude as the size of the depletion zone. Three-dimensional effects have to be considered to model the concentration profiles [65]. Although a complete study of these diffusoconvective growth regimes is out of the scope of this paper, we would like to comment on the different length scales relevant for thick cells.

If we look more precisely to the concentration profile near the tip of one branch [Fig. 11(b)], we notice a sharp increase of the concentration gradient at about 100 μm distance from the tip. In a study of zinc electrodeposition in 250 μm gap cells, we have already reported the existence of two zones in the depletion layer prior to the interfacial instability [70], a small band (100 μm scale) close to the electrode corresponding to the edge of the convective roll where the velocity of fluid is essentially vertical (the component of the fluid velocity along the growth direction is negligible), and a large scale zone (mm scale) corresponding to the main part of the convective roll where the concentration profile (averaged along the direction perpendicular to the glass plates) is quasilinear. This large scale zone increases as a square root of time during the depletion regime and stabilizes when the interfacial velocity becomes constant. If we try to define a diffusion length, it should correspond to the quiescent zone, that is the small band close to the electrode where diffusion and migration supply the ions to the interface. This length scale does not correspond to the wavelength of the pattern shown in Fig. 11. In free convection regimes, the interfacial dynamics and macroscopic patterns are determined by the whole concentration field and not only by its shape very close to the tip.

V. CONCLUSION

We have proposed here an original study of the internal structure of DBM obtained from copper acetate solutions in very thin gap cells, where the electrochemical deposition process is driven by diffusion. Two important issues have been reported. The first is the fact that the macroscopic characteristic lengths of the deposit (wavelength, branch width, fluctuation in the branch height) are roughly of the same order as the diffusion length. The second issue is that no wavelength selection in the strict sense of the term occurs during steady electrochemical growth (at least within a time interval much longer than the characteristic relaxation time of the concentration field). In particular, the internal structure of DBM can be either periodic or aperiodic. We have observed dynamical transitions between different periodic structures, which occur randomly during the growth. On the other hand, the metal concentration inside a finger depends neither on the current nor on the bulk concentration for a given counter anion. Despite the fact that the ratio of the finger width to the finger spacing is selected, these two quantities can vary during the growth, or from experiment to experiment. This approach is finally generalized to growth in thicker cells, in which diffusion, migration, and natural convection contribute to the transport of ionic species. In that case too we show that the largest length of the depletion layer sets the scale for the spacing between the branches.

ACKNOWLEDGMENTS

We thank Y. Sorin, G. Gadret, and L. Potin for their participation in the interferometric experiment elaboration. We are very grateful to G. Faivre, B. Nkonga, M. Z. Bazant, A. Arneodo, and L. Servant for stimulating discussions. We thankfully acknowledge support from the Centre National des Etudes Spatiales (CNES) under Grant No. 793/98/CNES/7315.

[1] M. Matsushita, M. Sano, Y. Hayakawa, H. Honjo, and Y. Sawada, Phys. Rev. Lett. **53**, 286 (1984).
[2] D. Grier, E. Ben-Jacob, R. Clarke, and L. Sander, Phys. Rev. Lett. **56**, 1264 (1986).
[3] Y. Sawada, A. Dougherty, and J. Gollub, Phys. Rev. Lett. **56**, 1260 (1986).
[4] P. Trigueros, J. Claret, F. Mas, and F. Sagues, J. Electroanal. Chem. Interfacial Electrochem. **219-235**, 165 (1991).
[5] L. Sander, in *The Physics of Structure Formation*, edited by W. Guttinger and G. Dangelmayr (Springer-Verlag, Berlin, 1987), pp. 257–266.
[6] F. Argoul, A. Arneodo, G. Grasseau, and H. Swinney, Phys. Rev. Lett. **61**, 2558 (1988).
[7] L. Lam, R. Pochy, and V. Castillo, in *Nonlinear Structures in Physical Systems. Pattern Formation, Chaos and Waves*, edited by L. Lam and H. Morris (Springer-Verlag, New York, 1990), pp. 11–31.
[8] J. Melrose, Chemom. Intell. Lab. Syst. **15**, 231 (1992).
[9] P. Garik, D. Barkey, E. Ben-Jacob, E. Bochner, N. Broxholm, B. Miller, B. Orr, and R. Zamir, Phys. Rev. Lett. **62**, 2703 (1989).
[10] D. Grier, D. Kessler, and L. Sander, Phys. Rev. Lett. **59**, 2315 (1987).
[11] D. Grier and D. Mueth, Phys. Rev. E **48**, 3841 (1993).
[12] J. Lin and D. Grier, Phys. Rev. E **54**, 2690 (1996).
[13] G. Kahanda and M. Tomkiewicz, J. Electrochem. Soc. **136**, 1497 (1989).
[14] Y. Sawada and H. Hyosu, Physica D **38**, 299 (1989).
[15] D. Hibbert and J. Melrose, Proc. R. Soc. London, Ser. A **432**, 149 (1989).

[16] J. Melrose and D. Hibbert, Phys. Rev. A **40**, 1727 (1989).
[17] J. Melrose, D. Hibbert, and R. Ball, Phys. Rev. Lett. **65**, 3009 (1990).
[18] V. Fleury, M. Rosso, J.-N. Chazalviel, and B. Sapoval, Phys. Rev. A **44**, 6693 (1991).
[19] D. Barkey, P. Garik, E. Ben-Jacob, B. Miller, and B. Orr, J. Electrochem. Soc. **139**, 1044 (1992).
[20] O. Zik and E. Moses, Phys. Rev. E **53**, 1760 (1996).
[21] M. Lopez-Salvans, F. Sagues, J. Claret, and J. Bassas, J. Electroanal. Chem. **421**, 205 (1997).
[22] M.-Q. Lopez-Salvans, F. Sagues, J. Claret, and J. Bassas, Phys. Rev. E **56**, 6869 (1997).
[23] F. Luborsky, J. Electrochem. Soc. **108**, 1138 (1961).
[24] S. Tajima and M. Ogata, Electrochim. Acta **13**, 1845 (1968).
[25] A. Bondarenko, Electrochim. Acta **29**, 887 (1984).
[26] E. Ben-Jacob and P. Garik, Nature (London) **343**, 523 (1990).
[27] E. Ben-Jacob, Contemp. Phys. **34**, 247 (1993).
[28] E. Ben-Jacob, G. Deutscher, P. Garik, N. Goldenfeld, and Y. Lareah, Phys. Rev. Lett. **57**, 1903 (1986).
[29] S. May and J. Maher, Phys. Rev. A **40**, 1723 (1989).
[30] C. Yeung and D. Jasnow, Phys. Rev. A **41**, 891 (1990).
[31] Y. Lereah, G. Deutscher, and E. Grunbaum, Phys. Rev. A **44**, 8316 (1991).
[32] H. Honjo and S. Ohta, Phys. Rev. A **45**, R8332 (1992).
[33] E. Ben-Jacob, Contemp. Phys. **38**, 205 (1997).
[34] J.-I. Wakita, I. Ràfols, H. Itoh, T. Matsuyama, and M. Matsushita, J. Phys. Soc. Jpn. **67**, 3630 (1998).
[35] O. Zik and E. Moses, Phys. Rev. E **60**, 518 (1999).
[36] O. Zik, Z. Olami, and E. Moses, Phys. Rev. Lett. **81**, 3868 (1998).
[37] F. Oberholtzer, D. Barkey, and Q. Wu, Phys. Rev. E **57**, 6955 (1998).
[38] D. Barkey, D. Watt, Z. Liu, and S. Raber, J. Electrochem. Soc. **141**, 1206 (1994).
[39] J. Huth, H. Swinney, W. McCormick, A. Kuhn, and F. Argoul, Phys. Rev. E **51**, 3444 (1995).
[40] V. Fleury, J.-N. Chazalviel, and M. Rosso, Phys. Rev. Lett. **68**, 2492 (1992).
[41] V. Fleury, J.-N. Chazalviel, and M. Rosso, Phys. Rev. E **48**, 1279 (1993).
[42] V. Fleury, J. Kaufman, and B. Hibbert, Phys. Rev. E **48**, 3831 (1993).
[43] V. Fleury, J. H. Kaufman, and D. B. Hibbert, Nature (London) **367**, 435 (1994).
[44] M. Wang, W. van Enckevort, N. Ming, and P. Bennema, Nature (London) **367**, 438 (1994).
[45] D. Barkey, J. Electrochem. Soc. **138**, 2912 (1991).
[46] P. Garik, J. Hetrick, B. Orr, D. Barkey, and E. Ben-Jacob, Phys. Rev. Lett. **66**, 1606 (1991).
[47] M. Bazant, Phys. Rev. E **52**, 1903 (1995).
[48] C. Léger, J. Elezgaray, and F. Argoul, Phys. Rev. E **58**, 7700 (1998).
[49] J.-N. Chazalviel, Phys. Rev. A **42**, 7355 (1990).
[50] P. Trigueros, F. Sagues, and J. Claret, Phys. Rev. E **49**, 4328 (1994).
[51] J. Newman, *Electrochemical Systems* (Prentice Hall, Englewood Cliff, NJ, 1991).
[52] R. Voss and M. Tomkiewicz, J. Electrochem. Soc. **132**, 371 (1985).
[53] R. Bower and S. Collins, Phys. Rev. A **43**, 3165 (1991).
[54] R. Smith and S. Collins, Phys. Rev. A **39**, 5409 (1989).
[55] J. Erlebacher, P. Searson, and K. Sieradzki, Phys. Rev. Lett. **71**, 3311 (1993).
[56] S. Hill and I. Alexander, Phys. Rev. E **56**, 4317 (1997).
[57] J. Elezgaray, C. Léger, and F. Argoul, Phys. Rev. Lett. (to be published).
[58] T. Witten and L. Sander, Phys. Rev. B **27**, 5686 (1983).
[59] P. P. Trigueros, J. Claret, F. Mas, and F. Sagués, J. Electroanal. Chem. **328**, 165 (1992).
[60] A. Kuhn and F. Argoul, Fractals **1**, 451 (1994).
[61] A. Kuhn and F. Argoul, J. Electroanal. Chem. **371**, 93 (1994).
[62] A. Kuhn and F. Argoul, Phys. Rev. E **49**, 4298 (1994).
[63] C. Léger, J. Elezgaray, and F. Argoul, Phys. Rev. Lett. **78**, 5010 (1997).
[64] J. Huth, Ph.D. thesis, The University of Texas at Austin, 1995.
[65] J.-N. Chazalviel, M. Rosso, E. Chassaing, and V. Fleury, J. Electroanal. Chem. **407**, 61 (1996).
[66] C. Léger, Ph.D. thesis, Université de Bordeaux I, 1999.
[67] C. Léger, J. Elezgaray, and F. Argoul, J. Electroanal. Chem. (to be published).
[68] Data translation frame grabber (768×512) and public domain NIH Image program, developed at the U.S. National Institutes of Health and available on the Internet at http://rsb.info.nih.gov/nih-image/.
[69] *Interferogram Analysis*, edited by D. Robinson and G. Reid (Institute of Physics Publishing, Techno House, Redcliffe Way, Bristol, BS1 6NX, England, 1993).
[70] F. Argoul, E. Freysz, A. Kuhn, C. Léger, and L. Potin, Phys. Rev. E **53**, 1777 (1996).
[71] F. Argoul, A. Arneodo, J. Elezgaray, and A. Kuhn, Fractals **5**, 75 (1997).
[72] P. Kurowski, C. Guthmann, and S. de Cheveigné, Phys. Rev. A **42**, 7368 (1990).
[73] M. Georgelin and A. Pocheau, Phys. Rev. E **57**, 3189 (1998).
[74] M. Ginibre, S. Akamatsu, and G. Faivre, Phys. Rev. E **56**, 780 (1997).
[75] S. Akamatsu and G. Faivre, Phys. Rev. E **58**, 3302 (1998).
[76] C. Wagner, J. Electrochem. Soc. **95**, 161 (1949).
[77] C. Tobias, J. Electrochem. Soc. **99**, 359 (1952).
[78] Y. Awakura, Y. Takenaka, and Y. Kondo, Electrochim. Acta **21**, 789 (1976).
[79] N. Ibl and O. Dossenbach, in *Comprehensive Treatise of Electrochemistry*, edited by J. Bockris, B. Conway, and E. Yeager (Plenum, New York, 1982), Vol. 16, pp. 133–237.
[80] V. Nechiporuk and I. Vinkler, Russ. J. Electrochem. **30**, 1271 (1994).
[81] G. Marshall and P. Mocskos, Phys. Rev. E **55**, 549 (1997).
[82] G. Marshall, P. Mocskos, H. Swinney, and J. Huth, Phys. Rev. E **59**, 2157 (1999).
[83] M. Rosso, J.-N. Chazalviel, V. Fleury, and E. Chassaing, Electrochim. Acta **39**, 507 (1994).
[84] M. Rosso, E. Chassaing, and J.-N. Chazalviel, Phys. Rev. E **59**, 3135 (1999).